Journal of Catalysis 392 (2020) 266–277

Contents lists available at ScienceDirect

Journal of Catalysis

journal homepage: www.elsevier.com/locate/jcat

Promoting effect of Fe on supported Ni catalysts in CO_2 methanation by *in situ* DRIFTS and DFT study

Huong Lan Huynh [a], Jie Zhu [b], Guanghui Zhang [b], Yongli Shen [d,*], Wakshum Mekonnen Tucho [c], Yi Ding [d], Zhixin Yu [a,*]

[a] Department of Energy and Petroleum Engineering, University of Stavanger, 4036 Stavanger, Norway
[b] State Key Laboratory of Fine Chemicals, PSU-DUT Joint Center for Energy Research, School of Chemical Engineering, Dalian University of Technology, Dalian 116024, China
[c] Department of Mechanical and Structural Engineering and Materials Science, University of Stavanger, 4036 Stavanger, Norway
[d] Tianjin Key Laboratory of Advanced Functional Porous Materials, Institute for New Energy Materials & Low-Carbon Technologies, School of Materials Science and Engineering, Tianjin University of Technology, Tianjin 300384, China

ARTICLE INFO

Article history:
Received 14 August 2020
Revised 12 October 2020
Accepted 13 October 2020
Available online 29 October 2020

Keywords:
CO_2 methanation
NiFe
In situ XRD
In situ DRIFTS
DFT calculation
Reaction mechanism

ABSTRACT

Bimetallic NiFe catalysts have emerged as a promising alternative to the traditional Ni catalysts for CO_2 methanation. However, the promoting effect of Fe on the bimetallic catalysts remains ambiguous. In this study, a series of NiFe catalysts derived from hydrotalcite precursors were investigated. *In situ* x-ray diffraction (XRD) analysis revealed that small NiFe alloy particles were formed and remained stable during reaction. When Fe/Ni = 0.25, the alloy catalysts exhibited the highest CO_2 conversion, CH_4 selectivity and stability in CO_2 methanation at low temperature of 250–350 °C. The *in situ* diffuse reflectance infrared Fourier transform spectroscopy (DRIFTS) study indicated that the formate pathway was the most plausible reaction scheme on both Ni and NiFe alloy catalysts, while a moderate addition of Fe facilitated the activation of CO_2 via hydrogenation to *HCOO. Density functional theory (DFT) calculations further demonstrated that the overall energy barrier for CH_4 formation was lower on the alloy surface.

1. Introduction

Chemical conversion of CO_2 into valuable products has been attractive to chemists ever since the advent of catalysis [1]. The discovery of CO_2 methanation (Sabatier reaction, Eq. (1)) in 1902, which converts CO_2 and H_2 into CH_4, has been crucial for the development of CO_2 conversion processes [2]. The potential for CO_2 mitigation and renewable energy storage has been demonstrated in the emerging Power-to-Gas (PtG) technology. In this concept, the synthetic or substitute natural gas (SNG) produced via the Sabatier process is considered as a promising chemical energy carrier for the surplus electricity produced from intermittent renewables such as wind and solar power [3–5].

$$CO_2 + 4H_2 \leftrightarrow CH_4 + 2H_2O \ \Delta H^{\circ}_{298K} = -165 \text{ kJ mol}^{-1} \quad (1)$$

$$CO_2 + H_2 \leftrightarrow CO + H_2O \ \Delta H^{\circ}_{298K} = 41 \text{ kJ mol}^{-1} \quad (2)$$

The molecular transformation of CO_2 is challenging since the molecule is well-known for its thermodynamic stability. Metal catalysts are therefore crucial to activate the closed-shell molecule [6]. At atmospheric pressure, CO_2 methanation and the reverse water–gas shift reaction (RWGS, Eq. (2)) occur simultaneously on group VIII metals. Although noble metals (e.g., Ru, Rh) are highly active, Ni-based catalysts are prominently exploited as methanation catalysts due to cost effectiveness. Considerable efforts have been devoted to improving the activity and stability of Ni-based catalysts at low temperatures (<350 °C) [7,8].

The addition of Fe to Ni has been reported as a promising strategy to achieve better catalytic performance and stability of methanation catalyst. It was first predicted by theoretical modeling, i.e., density functional theory (DFT) simulations. Based on the calculated energies, NiFe and Ni_3Fe showed excellent activity compare to Ni and Fe, close to that of the best catalysts (i.e., Ru and Co) [9,10]. Experimental investigations have also verified that NiFe catalysts exhibited higher activity than their individual constituent in CO_2 hydrogenation (H_2/CO_2 = 91/9) at 250 °C [11]. The bimetallic NiFe catalytic system is very attractive because cheap Fe will further contribute to the cost-effectiveness of the Ni-based methanation catalysts.

Studies on NiFe catalysts for CO_2 methanation have been reported on different catalytic supports, i.e., Al_2O_3 [12], TiO_2, SiO_2, Nb_2O_5, and ZrO_2 [13,14], while unsupported NiFe catalysts were also investigated [15]. The optimal composition of Fe in

* Corresponding authors.
E-mail addresses: ylshen@tjut.edu.cn (Y. Shen), zhixin.yu@uis.no (Z. Yu).

https://doi.org/10.1016/j.jcat.2020.10.018
0021-9517/

Ni-based catalysts to achieve the promoting effect appears to be dependent on the support type and metal loading. Importantly, the amount of Fe addition plays a crucial role since a small amount of Fe boosted the production of CH_4 while large amount of Fe promoted the formation of CO via RWGS reaction [16]. NiFe catalysts prepared from layered double hydroxides (LDH) materials were also studied [17,18]. Overall, most of these studies have confirmed the superiority of NiFe alloy catalysts in CO_2 methanation compared to monometallic Ni catalysts. Regardless of metal loading or type of supports, the optimal Fe content has been reported with a Fe/Ni molar ratio up to 1/3. Besides, the Ni_3Fe/Al_2O_3 catalysts showed a more stable performance compared to commercial Ni methanation catalysts [19]. Based on kinetic measurements, Mutz *et al.* assumed the effect of Fe could be due to the synergetic effect of NiFe alloy [19]. While the CO dissociation energy was used as a descriptor for CO and CO_2 methanation activity [9,17], the binding energy of adsorbed CO was proposed as the key descriptor for CO_2 hydrogenation to CH_4 (H_2/CO_2 = 2) [16]. An improvement in CO_2 uptake capacity on alloy surfaces corresponding to the promoted CH_4 production has also been speculated [20]. Nevertheless, there is no consensus on the promotional effect of Fe on Ni, while the mechanism of CO_2 methanation on NiFe alloy catalysts is not clearly understood.

Insights at the atomic scale of active intermediates and key elementary reaction steps are essential to unravel the reaction mechanism of catalytic reaction. In this work, we attempted to understand the role of Fe and the reaction mechanism by *in situ* X-ray diffraction (XRD) and *in situ* diffuse reflectance infrared Fourier transform spectroscopy (DRIFTS) study combined with DFT simulations. To the best of our knowledge, this is the first combined experimental and theoretical study on NiFe alloy catalysts for the Sabatier reaction. We prepared a series of NiFe on (Mg,Al)O_x supported catalysts derived from hydrotalcite (HT) precursors in order to study the impact of Fe content on the physicochemical properties and catalytic performance in CO_2 methanation. The formation of NiFe alloy upon reduction, as well as the structural changes during reaction was investigated by *in situ* XRD analysis.

2. Experimental

2.1. Catalyst synthesis

A series of NiFe/(Mg,Al)O_x catalysts were prepared by calcination of HT precursors. The precursors were synthesized by rapid coprecipitation reported in our previous work [21]. In a typical synthesis, a metal nitrate solution (1 M) containing a calculated amount of Ni$(NO_3)_2{\cdot}6H_2O$, Fe$(NO_3)_3{\cdot}9H_2O$, Mg$(NO_3)_2{\cdot}6H_2O$ and Al$(NO_3)_3{\cdot}9H_2O$ were quickly injected to a base solution of NaOH and Na_2CO_3 under vigorous stirring at 60 °C. The mixture was aged at 85 °C for 18 h. The calcination of the as-prepared precursors was conducted at 600 °C for 6 h in flowing synthetic air. In all the catalysts, the (Ni + Mg)/(Al + Fe) molar ratio was fixed at 3 and the Ni loading was kept constant at 20 wt%. The calcined catalysts were denoted as NiFe-*x*, where *x* is the Fe/Ni molar ratio that varies from 0 to 0.5 (Table 1).

2.2. Catalyst characterization

The elemental compositions of the calcined catalysts were analyzed by inductively coupled plasma optical emission spectrometry (ICP-OES) using OPTIMA 4300 DV (PerkinElmer) instrument. The dried samples were dissolved in a mixture of HCl and HNO_3 at a ratio of 3 and further diluted for analysis.

Crystallographic information of the as-prepared and calcined catalysts was determined by X-ray diffraction. The *ex situ* XRD patterns were recorded on D8 Advance (Bruker) micro-diffractometer using CuKα radiation source with a step interval of 1° min^{-1}.

Nitrogen physisorption was performed in a Tristar 3000 (Micromeritics) instrument at −196 °C. Prior to analysis, all samples were degassed at 150 °C under vacuum overnight. The specific surface area of the catalysts was calculated using Brunauer-Emmett-Teller (BET) method, while the pore volume and pore size distributions were evaluated using Barrett-Joyner-Halenda (BJH) models.

Temperature-programmed reduction (TPR) of the calcined catalysts and temperature-programmed desorption (TPD) of the reduced catalysts were performed on AutoChem II 2920 (Micromeritics). In a typical measurement, 100 mg of calcined sample was used to obtain reliable data [22]. The calcined catalysts were degassed, then the analysis was carried out by heating the sample from 50 °C to 950 °C at a heating rate of 10 K min^{-1} in 10 vol% H_2/Ar (50 mL min^{-1}). Subsequently, the sample was purged with He flow at 600 °C for 30 min and cooled down to 50 °C. Thereafter, the sample was exposed to a flow of 6 vol% CO_2/Ar (50 mL min^{-1}) for 1 h, followed by purging in He for another 1 h to remove weakly adsorbed CO_2. Finally, CO_2-TPD data were recorded by heating the sample to 800 °C at a heating rate of 10 K min^{-1} in flowing He.

Hydrogen chemisorption analysis was conducted in ASAP 2020 Plus (Micromeritics) instrument at 35 °C. In a typical experiment, 200 mg of calcined catalyst was reduced in H_2 flow at 600 °C for 4 h with a heating rate of 5 K min^{-1} and cooled down to 35 °C in flowing He. It was assumed that the chemisorption of H_2 occurred only on Ni atom with a dissociative mechanism because Fe is known to be inactive in H_2 chemisorption.

The morphology and particle size of the reduced-passivated and spent catalysts were revealed by transmission electron microscopy (TEM) analysis using JEM-2100 Plus (JEOL) microscope operating at 200 kV. The calcined catalysts were reduced in 50 vol% H_2/N_2 (100 mL min^{-1}, STP) at 600 °C for 4 h (heating rate of 5 K min^{-1}) in a fixed-bed reactor. The sample was cooled down in a flowing N_2 to room temperature before being passivated by adding synthetic air to the gas mixture. The oxygen content was adjusted to 0.1 vol% and slowly increased to 1 vol%.

2.3. CO_2 methanation tests

The catalytic performance was evaluated on a stainless-steel tubular fixed-bed reactor as reported in our previous work [21]. In a typical experiment, 60 mg of calcined catalyst (200–355 μm) was diluted with 600 mg of SiC (ca. 355 μm). The catalyst was reduced using 50 vol% H_2/N_2 (100 mL min^{-1}, STP) at 600 °C for 4 h (heating rate of 5 K min^{-1}). The temperature-dependent activity tests were carried out at a temperature interval of 200–450 °C at a heating rate of 1 K min^{-1}. The condition was held for 1 h at each temperature to obtain a stable CO_2 conversion. The total flow rate of reactant gases ($H_2/CO_2/N_2$ vol.% = 64/16/20) was 270 mL min^{-1} (STP), which corresponding to a weight hourly space velocity (WHSV) of 43,200 mL_{CO2} $g_{cat}^{-1}h^{-1}$ or a gas hourly space velocity (GHSV) of 34,000 h^{-1}.

For long-term stability evaluation, the catalysts were tested at 300 °C for more than 60 h of time on stream (TOS). Moreover, a blank test was conducted to confirm the inert nature of SiC in the stainless-steel reactor under reaction condition. The conversion of CO_2 and product selectivity were defined following Eq. (3) and Eq. (4), where F^{in} and F^{out} are the molar flow rates (mol h^{-1}).

$$X_{CO2}(\%) = \frac{F_{CO2}^{in} - F_{CO2}^{out}}{F_{CO2}^{in}} \times 100 \quad (3)$$

$$S_i(\%) = \frac{F_i^{out}}{F_{CO2}^{in} - F_{CO2}^{out}} \times 100 \quad (4)$$

Table 1
Elemental compositions and textural properties of calcined catalysts.

Catalyst	Nominal Fe/Ni molar ratio	ICP-OES analysis			N_2 physisorption of calcined catalyst		
		Ni [wt %]	Fe [wt %]	Fe/Ni molar ratio	BET Specific surface area [m^2 g^{-1}]	BJH Pore volume [cm^3 g^{-1}]	BJH Average pore size [nm]
NiFe-0	0	19.85	0	0	227.8	0.73	10.1
NiFe-0.1	0.1	19.84	1.87	0.1	240.0	0.77	11.0
NiFe-0.25	0.25	19.62	4.70	0.25	232.6	0.70	9.7
NiFe-0.33	0.33	18.83	6.39	0.36	247.3	0.72	9.7
NiFe-0.5	0.5	19.50	9.45	0.51	197.4	0.68	10.5

2.4. In situ XRD study

In situ XRD diffractograms were collected on a SmartLab 9 kW (Rigaku) diffractometer equipped with an XRK900 reactor chamber and a 1D/Dtex detector to improve the signal-to-noise ratio. The diffractometer was operated at 45 kV and 200 mA using CuKα radiation source. About 50 mg of calcined catalyst was loaded in the sample holder and heated up to 600 °C at a heating rate of 10 K min^{-1} under a flow of pure H_2 (30 mL min^{-1}) for reduction at atmospheric pressure. The diffractograms were subsequently recorded at 100–600 °C at a scanning speed of 8° min^{-1} (hold for 5 min at each temperature). When the temperature reached 600 °C, the data were collected every 15 min for 90 min. The *in situ* XRD measurement was also conducted under reaction conditions. A gas mixture of $CO_2/H_2/N_2$ = 17/69/14 (30 mL min^{-1}) was introduced after cooling the reduced sample down to 200 °C. The XRD diffractograms were continuously recorded at elevated temperatures.

2.5. In situ DRIFTS study

In situ DRIFTS was conducted on a Nicolet iS 50 (Thermo Scientific) FTIR spectrometer equipped with a mercury cadmium telluride detector cooled by liquid N_2. Prior to measurement, the calcined catalysts were reduced in 30% H_2/N_2 flow at 600 °C for 90 min (heating rate of 10 K min^{-1}). Thereafter, the sample was cooled down to 200 °C followed by N_2 purging for 10 min. For CO_2 adsorption study, a flow of CO_2/N_2 at a ratio of 1/5 (6 mL min^{-1}) was introduced. For CO_2 methanation study, a gas mixture of $CO_2/H_2/N_2$ at a ratio of 1/4/5 was used. The *in situ* DRIFTS spectra were continuously collected at elevated temperatures.

2.6. DFT calculations

Spin-unrestricted calculations were performed using DFT-D scheme provided by DMol3 code [23,24]. The exchange–correlation functional was expressed using the generalized gradient approximation (GGA)-Perdew, Burke, and Ernzerhof (PBE) functional [25]. The Ni(1 1 1) and Ni4Fe(1 1 1) alloy were modeled using five-layered slab of (3 × 3) surface unit cell. In the Ni4Fe catalyst, Ni atoms were replaced with Fe atoms with a Fe/Ni ratio of ¼, representing NiFe-0.25 catalyst. A vacuum region was set to be 30 Å between repeated slabs. In our calculations, the atoms in the bottom two layers were fixed at their bulk position and those in the top three layers together with the adsorbates are allowed to relax. Double numerical plus polarization (DNP) basis set was used throughout the calculation. The convergence criteria were set to be 1×10^{-5} Ha, 0.001 Ha $Å^{-1}$, and 0.005 Å for energy, force, and displacement convergence, respectively. A self-consistent field (SCF) density convergence with a threshold value of 1×10^{-5} Ha was specified. K-points were sampled using the 4 × 4 × 1 Monkhorst-Pack mesh for Ni and NiFe alloys.

All the transition states (TS) were determined using the linear synchronous transit (LST) and quadratic synchronous transit (QST) methods. The TS structures were confirmed by using a local minimum search (after a small distortion of each TS in the reaction coordinate direction) to reach the reactants and products [26]. The desorption energy (E_{des}) of adsorbed species was calculated with Eq. (5), where E_{ads} and E_{surf} are the total energies of the isolated adsorbates in vacuum and the clean surface, respectively. E_{ads_surf} is the total energy of the adsorbed system.

$$E_{des} = E_{surf} + E_{ads} - E_{ads_{surf}} \quad (5)$$

3. Results and discussion

3.1. Physicochemical properties

XRD diffractograms of the as-prepared HT precursors show the characteristic diffractions of pure HT with layered structures in rhombohedral 3R symmetry (**Figure S1**). Based on calculated lattice parameters (**Table S1**), it is confirmed that pure crystalline Ni-Fe-Mg-Al HT precursors were successfully synthesized via the rapid coprecipitation method. After calcination at 600 °C, the precursors fully decomposed into mixed metal oxides (Fig. 1). The diffraction patterns of bimetallic NiFe catalysts were similar to monometallic NiFe-0 catalyst and were dominated by the reflections of not only NiO (JCPDS 01–089-5881) but also MgO (JCPDS 03–065-0476) and Al_2O_3 (JCPDS 01–073-1512). It has been reported that at a moderate calcination temperature of 600 °C, only

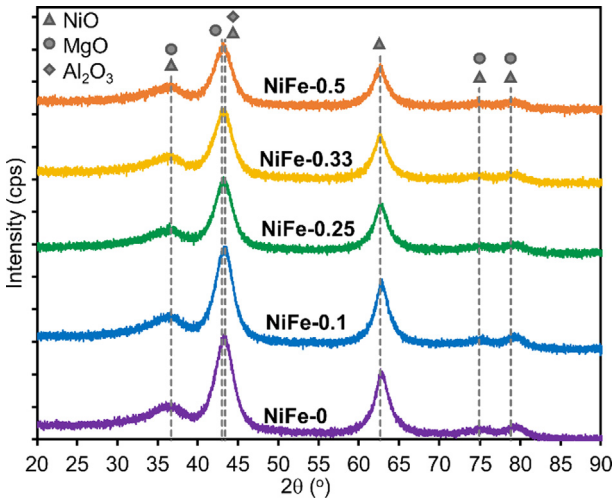

Fig. 1. XRD diffractograms of the calcined catalysts.

the rock-salt-type phase (NiO or MgO) was observed while crystalline spinels (e.g., $MgAl_2O_4$) would be formed at above 800 °C [27]. Therefore, it is assumed that the support was in the mixed oxide phase $(Mg,Al)O_x$. Notably, the increase of Fe resulted in poorer crystallinity with slightly smaller crystallite sizes of the oxide catalysts, as can be seen by the reduced intensity of the diffraction lines (Fig. 1).

Elemental analysis by ICP-OES of the calcined catalysts reveals the actual metal loading and Fe/Ni molar ratio, which was close to the nominal values (Table 1). It could be assumed that Ni and Fe ions were successfully precipitated.

The N_2 physisorption analysis of calcined catalysts shows that all isotherms were type IV with hysteresis loop at high P/P_o range (**Figure S2**), attributed to mesoporous materials according to IUPAC classification [28]. The pore size distribution of calcined catalysts (**Figure S3**) further confirmed that the calcined catalysts had mesopores in the range of 10–15 nm. In general, all HT-derived catalysts had a relatively high surface area of 200–250 $m^2\ g^{-1}$ and a large pore volume of 0.7–0.8 $cm^3\ g^{-1}$ (Table 1). Interestingly, the increase of Fe content did not significantly affect the mesoporous texture of the catalysts.

3.2. Temperature programmed reduction and in situ XRD study

The reduction behavior of calcined catalysts was investigated by H_2-TPR analysis (Fig. 2). For the monometallic NiFe-0 catalyst, only a single reduction peak at 810 °C was observed, corresponding to the reduction of NiO to metallic Ni. In fact, the reduction temperature of pure NiO is at 290–340 °C [29]. Other types of Ni^{2+} cations such as NiO aggregates or freely bounded NiO were not depicted. It has been suggested that Ni was embedded in the $MgO\text{-}Al_2O_3$ structure, thus it was harder to be reduced [29,30]. For bimetallic NiFe catalysts, the sequential reduction of Fe_2O_3 was not observed due to low Fe content [31,32], and only small peaks at 350–400 °C were observed in Fe-rich catalysts. This could be ascribed to the partial reduction of Fe_2O_3 to Fe_3O_4 [19,33], whereas the reduction of Fe_3O_4 to Fe and NiO to Ni was overlapped at higher temperatures [31,32]. The main reduction peaks of Ni species shifted to lower temperatures with increasing Fe content. Therefore, it can be suggested that Fe enhanced the reducibility of the NiFe alloy catalysts.

The *in situ* XRD diffractograms of NiFe-0, NiFe-0.25, and NiFe-0.5 catalysts during reduction are shown in Fig. 3. For the monometallic catalyst, the diffraction line associated with metallic

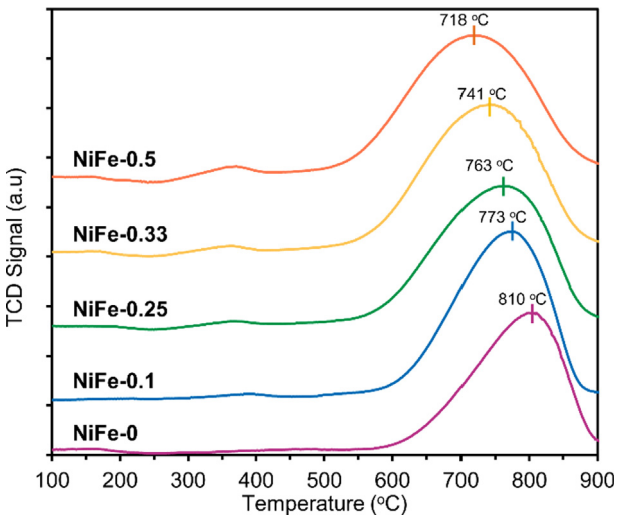

Fig. 2. H_2-TPR profiles of the calcined catalysts.

Ni(200) was detected at 2θ of 51.4° (JCPDS 03–065-2865) after the sample reached 600 °C for 15 min. The intensity of this line gradually increased during 90 min of reduction, indicating the growth of Ni particle from 5.3 nm to 9.1 nm (**Table S2**). Besides, the mixed oxides phases $(Mg,Al)O_x$ remained unchanged, demonstrating their irreducible nature. As for the NiFe-0.25 and NiFe-0.5 catalysts, the characteristic peak shifted to a lower angle of 50.85° and 50.75°, respectively. Correspondingly, the d-spacing obtained from the (200) reflection was in a linear correlation with the molar ratio of Ni/(Ni + Fe) (Figure S4) [34]. The lattice parameter appeared to be increased with increasing Fe content. The shift in peak position could confirm the formation of Ni-rich NiFe fcc alloy upon reduction of NiFe-0.25 and NiFe-0.5 catalysts at 600 °C [19,34–36]. Moreover, the alloy crystals were smaller in size (5–6 nm) than Ni crystals (9 nm) (**Table S2**).

3.3. Metal surface area and basicity of the reduced catalysts

The maximum Ni surface area of 5.52 $m^2\ g^{-1}$ was obtained from NiFe-0 catalyst based on H_2 chemisorption analysis. With increasing Fe content, the Ni surface area dramatically dropped to 0.1 $m^2\ g^{-1}$ for NiFe-0.5 catalyst although the Ni loading was kept constant at 20 wt% (Table 2). These results further confirmed the formation of NiFe alloy which is inactive in H_2 chemisorption [34].

CO_2-TPD analysis showed that the alloy catalysts exhibited stronger basicity than monometallic catalyst, due to the larger integrated area of the desorption profiles (**Figure S5**). It reveals that Fe addition could enhance the total basicity of the catalysts. However, the impact of different basic types (i.e., weak, medium, and strong) on the catalytic activity in CO_2 methanation remains disputable [37,38].

3.4. CO_2 methanation activity tests

3.4.1. Temperature-programmed reaction study

The catalytic behavior of different NiFe catalysts was firstly studied in temperature-programmed reaction at atmospheric pressure. It shows that NiFe alloy catalysts were more active than monometallic Ni catalysts in CO_2 methanation at low temperatures, particularly at 260–290 °C (Fig. 4**.a**). NiFe-0.25 achieved the highest CO_2 conversion of 53% at 270 °C. As the temperature increased to 450 °C, a decline of activity for all catalysts was observed.

During CO_2 methanation, the simultaneous RWGS reaction led to a competition between CO and CH_4 formation. At 250 °C, the highest CH_4 selectivity was obtained from the NiFe-0 catalyst (Fig. 4**.b**). However, at 270–400 °C, NiFe alloy catalysts exhibited better CH_4 selectivity, particularly for NiFe-0.25 with S_{CH4} greater than 97%. At a higher temperature of 400–450 °C, a decrease of S_{CH4} was observed because the endothermic RWGS reaction was favored. Moreover, the addition of too large amount of Fe facilitated the formation of CO for NiFe-0.33 and NiFe-0.5. It has been reported that although $Fe/(Mg,Al)O_x$ catalysts had very low activity in CO_2 methanation, the CO selectivity was very high (~100%) [17]. Fe-rich Ni/ZrO_2 catalysts have also been found to significantly promote the RWGS reaction rather than CO_2 methanation [16]. Hence, it could be concluded that a high CH_4 yield could only be achieved over a suitable composition of Ni and Fe, particularly the NiFe-0.25 catalyst in the low-temperature region.

3.4.2. Long-term activity test

The best performing NiFe-0.25 catalyst was tested in CO_2 methanation under high GHSV condition for more than 100 h of TOS at 300 °C. The formation rate of CH_4 was higher over NiFe-0.25 alloy catalyst compared to the monometallic NiFe-0 catalyst

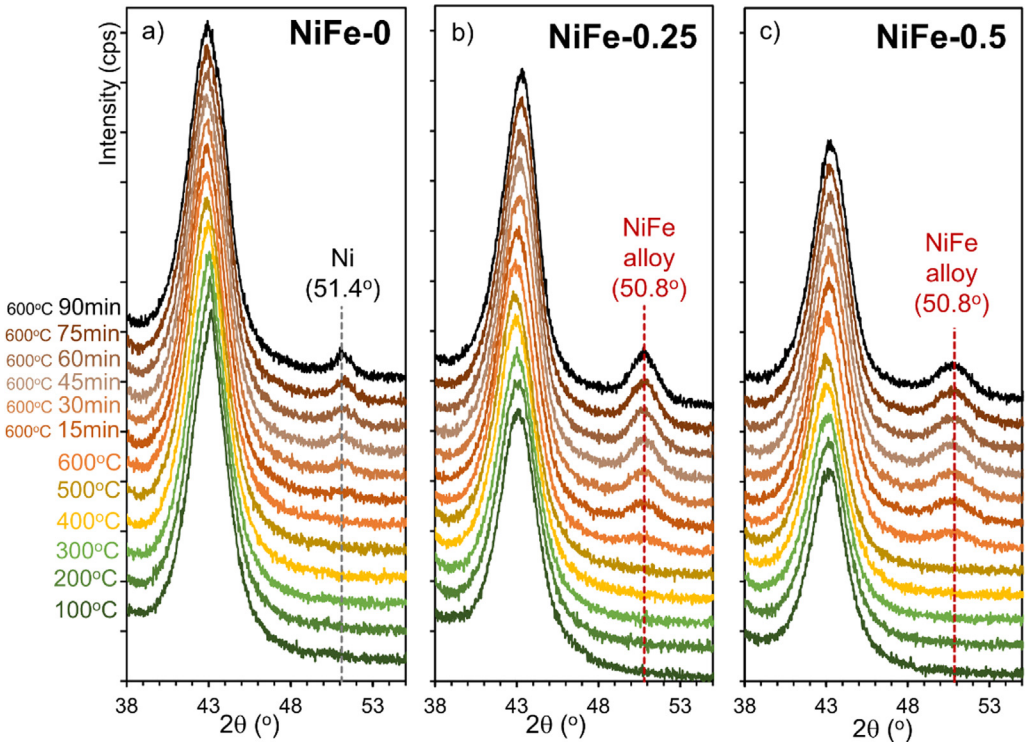

Fig. 3. *In situ* XRD diffractograms of (a) NiFe-0, (b) NiFe-0.25, and (c) NiFe-0.5 catalysts during reduction in pure H_2 at increasing temperatures and time.

Table 2
H_2 chemisorption uptake and Ni surface area of reduced catalysts.

Samples	H_2 chemisorption uptake [μmol g_{cat}^{-1}]	Metal surface area [m^2 g^{-1}]
NiFe-0	70.6	5.52
NiFe-0.1	50.1	3.91
NiFe-0.25	29.4	2.30
NiFe-0.33	16.4	1.28
NiFe-0.5	1.3	0.10

(Fig. 5). A slight decline in CO_2 conversion with 0.18% h^{-1} for NiFe-0 and 0.08% h^{-1} for NiFe-0.25 was observed. Both catalysts exhibited high stability and the deactivation rate was low compared to those reported in literature [19].

3.4.3. Catalyst deactivation study

The TEM images of NiFe-0 and NiFe-0.25 reduced-passivated catalysts show that metallic particles (Ni and NiFe alloy) were well dispersed on the support (Fig. 6.**a** and Fig. 6.**b**). The average particle sizes were close at 6.7 ± 1.8 nm and 6.1 ± 1.5 nm. The TEM images of catalysts after long-term tests were also examined (Fig. 6.**c** and Fig. 6.**d**). The average particle sizes of the spent catalysts remained constant at 6.7 ± 1.4 nm and 6.1 ± 2.2 nm for NiFe-0 and NiFe-0.25, respectively. Since carbonaceous species were not observed, carbon formation, as well as metal sintering, are not the reason for the degradation of methanation activity.

In situ XRD analysis was further used to study the phase changes during CO_2 methanation at increasing temperatures. In addition to previously identified mixed oxides and Ni or NiFe

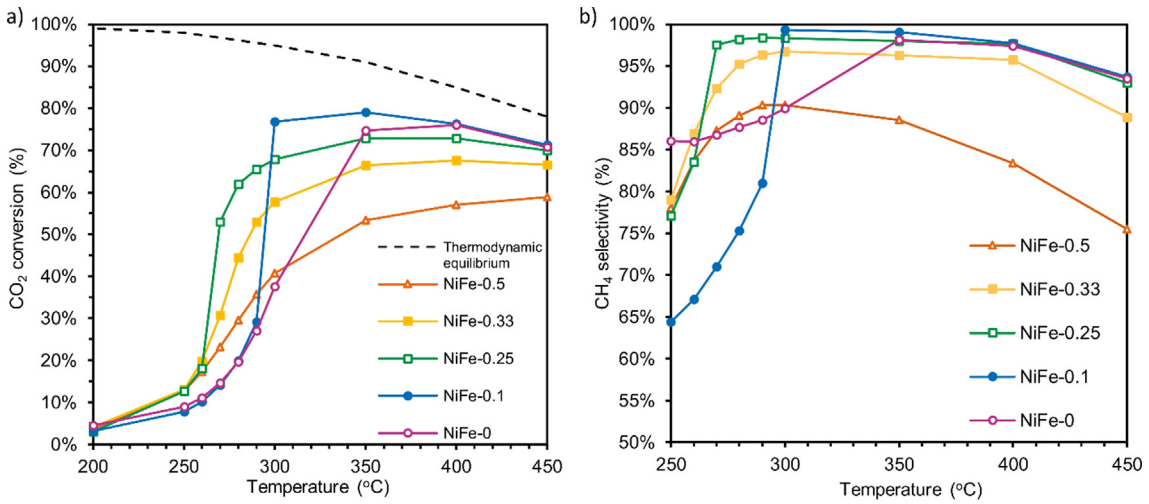

Fig. 4. (a) CO_2 conversion and (b) CH_4 selectivity as a function of reaction temperature in CO_2 methanation ($H_2/CO_2/N_2$ vol.% = 64/16/20, WHSV = 43,200 mL_{CO2} g_{cat}^{-1} h^{-1}).

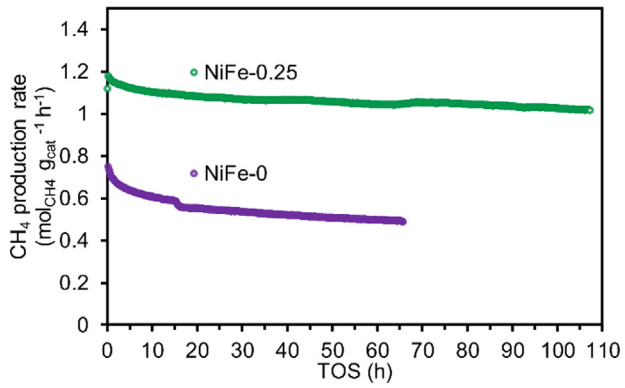

Fig. 5. Methane production rate over NiFe-0.25 and NiFe-0 catalysts during long-term test at 300 °C ($H_2/CO_2/N_2$ vol.% = 64/16/20, WHSV = 43,200 mL_{CO2} $g_{cat}^{-1}h^{-1}$).

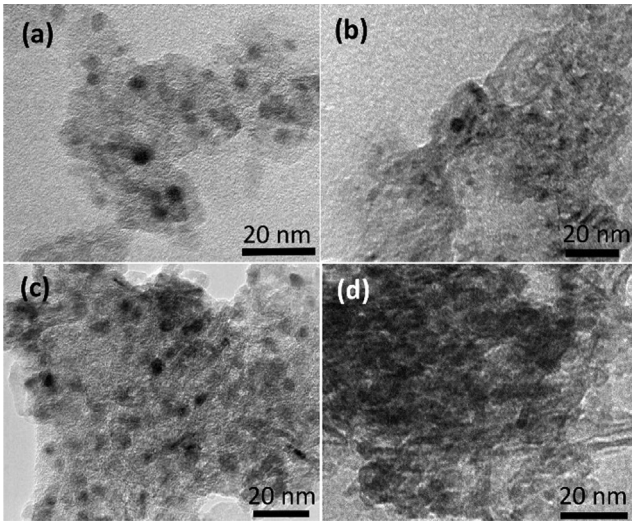

Fig. 6. TEM images of (a) reduced-passivated NiFe-0, (b) reduced-passivated NiFe-0.25, (c) spent NiFe-0 and (d) spent NiFe-0.25 catalysts after the long-term stability test.

phases, no carbon formation was observed in the *in situ* XRD diffractograms (**Figure S6**). The crystallite size of Ni and NiFe alloy particles were almost unchanged during reaction at 200–350 °C. NiFe-0 catalyst maintained its metal crystallite size of approximately 9 nm, whereas NiFe alloy crystallite size was stable in the range of 5–6 nm under reaction conditions at increasing temperatures (**Table S2**).

Furthermore, time-resolved *in situ* DRIFTS spectra during CO_2 methanation were also recorded at 300 °C for 180 min over NiFe-0 catalysts (**Figure S7**). While the intensity of vibration bands attributed to gaseous CH_4 species gradually reduced, linearly adsorbed *CO species on Ni was not detected during reaction. As a result, the presence of nickel carbonyl could not be confirmed [39]. Overall, metal sintering, carbon, and nickel carbonyl formation were likely not the reasons for catalyst deactivation on both Ni and NiFe alloy catalysts.

3.5. In situ DRIFTS study

3.5.1. In situ DRIFTS of CO_2 adsorption

To identify the surface species on catalysts during CO_2 adsorption, the sample was *in situ* reduced before exposure to CO_2 at increasing temperatures. The *in situ* DRIFTS spectra over NiFe-0 catalyst show intense IR bands of gaseous linearly adsorbed $*CO_2$ at 2350 cm^{-1}, as well as the surface *OH species at 3600–3700 cm^{-1} (Fig. 7**.a**). It is worth noting that $*OH^-$ could be produced during the reduction of catalysts [40]. The IR bands at 1223, 1395–1405 and 1668 cm^{-1} are characteristic of surface $*CO_2$ species, namely bicarbonate $*HCO_3^-$ (1220 and 1650 cm^{-1}) and monodentate carbonate $*CO_3$ (1360–1400 cm^{-1}). As the temperature increases, the intensity of $*HCO_3$ bands at 1223 and 1668 cm^{-1} gradually decreased, while the band of $*CO_3$ species only slightly reduced. Monodentate $*CO_3$ species were assumed to adsorb on strong basic sites of the catalyst, more stable and harder to remove at high temperatures. As for Ni-based on (Mg, Al)O_x catalysts, it is anticipated that surface *OH species possibly provided weak basic sites to produce $*HCO_3$, whereas *O species with strong basic site facilitated the formation of monodentate $*CO_3$ [41].

In addition, similar surface species were detected over the NiFe-0.25 catalyst (Fig. 7**.b**). Nevertheless, the most significant difference was the transition of $*HCO_3$ vibration bands to formate-related bands over NiFe alloy catalysts, but not on NiFe-0 catalyst. The IR bands at 1605 cm^{-1} were ascribed to *HCOO species [42–44]. The formate species started to appear at 290 °C, while the band intensity of HCO_3^- was decreased. Likewise, the *HCOO species on NiFe-0.5 was detected at an even lower temperature of 250 °C (**Figure S8**). It is suggested that NiFe alloy provided a synergistic effect in the transformation of $*HCO_3$ to formate species.

Moreover, linearly adsorbed *CO species on Ni surface (small IR bands at 2035 cm^{-1}) were detected at 200 °C but disappeared at higher temperatures of 250–350 °C. On the other hand, both linear and gaseous *CO species were found on the alloy catalysts (IR bands at 2210 cm^{-1}), especially on the Fe-rich NiFe-0.5 catalyst (**Figure S8**). As the Fe content increased, a larger amount of gaseous *CO on the alloy surface was observed. This observation is in good agreement with previous reports that the binding energy of *CO was weaker on NiFe alloy compared to Ni surface, thus *CO was desorbed easier [16,45]. It can be speculated that the activation of $*CO_2$ via direct dissociation was promoted on NiFe alloy surface compared to that on Ni surface. A DFT study has also reported that CO_2 activation by decomposition to *CO and *O was easier on Ni_3Fe surface than monometallic Ni surface [34].

3.5.2. In situ DRIFTS of CO_2 methanation

In situ DRIFTS spectra of NiFe-0 and NiFe-0.25 catalysts during CO_2 methanation (H_2/CO_2 = 4) are presented in Fig. 8. The C-H stretching vibrations of $*CH_4$ were observed at 3015 and 1305 cm^{-1}. The $*CH_4$ vibration on NiFe-0.25 appeared at low temperature of 200 °C, while the band intensity was always higher than on NiFe-0 at the same temperature. This further proves that the NiFe-0.25 catalyst performed higher activity in CO_2 methanation, in accordance with the temperature-dependent activity test results. Similar to the *in situ* DRIFTS spectra during CO_2 adsorption, $*CO_3$, $*HCO_3$, gaseous $*CO_2$, and *OH species were all detected.

As the temperature increased, a transition from $*HCO_3$ (1665 cm^{-1}) to *HCOO (1605 cm^{-1}) was observed over both catalysts. Small bands at 2855 cm^{-1} were attributed to the C-H stretching vibration from *HCOO species [46]. For NiFe-0, the peak of $*HCO_3$ (at 1665 and 1223 cm^{-1}) decreased and disappeared at 300 °C, accompanied by the increase in intensity of *HCOO (at 1605 and 2855 cm^{-1}). For NiFe-0.25 catalyst, the disappearance of $*HCO_3$ readily occurred at 280 °C. Moreover, the IR bands at 2735 cm^{-1} could also be assigned to aldehyde hydrogen (formyl) *HCO species [47,48].

Therefore, a formate pathway is highly plausible for CO_2 methanation of over Ni and NiFe alloy catalysts on (Mg,Al)O_x support. The addition of Fe to Ni-based catalysts would not interfere with this pathway since similar surface species were observed. The transition of $*HCO_3$ to *HCOO observed on both catalytic surfaces was

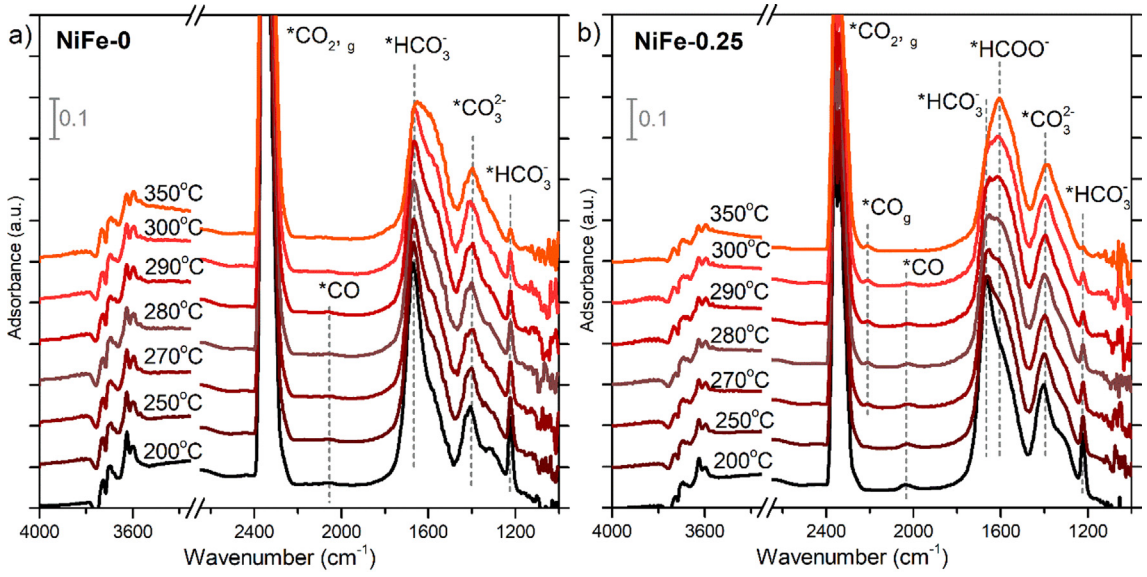

Fig. 7. *In situ* DRIFTS spectra of (a) NiFe-0 and (b) NiFe-0.25 catalysts under CO_2 adsorption condition (CO_2/N_2 vol.% = 1/5) at increasing temperatures.

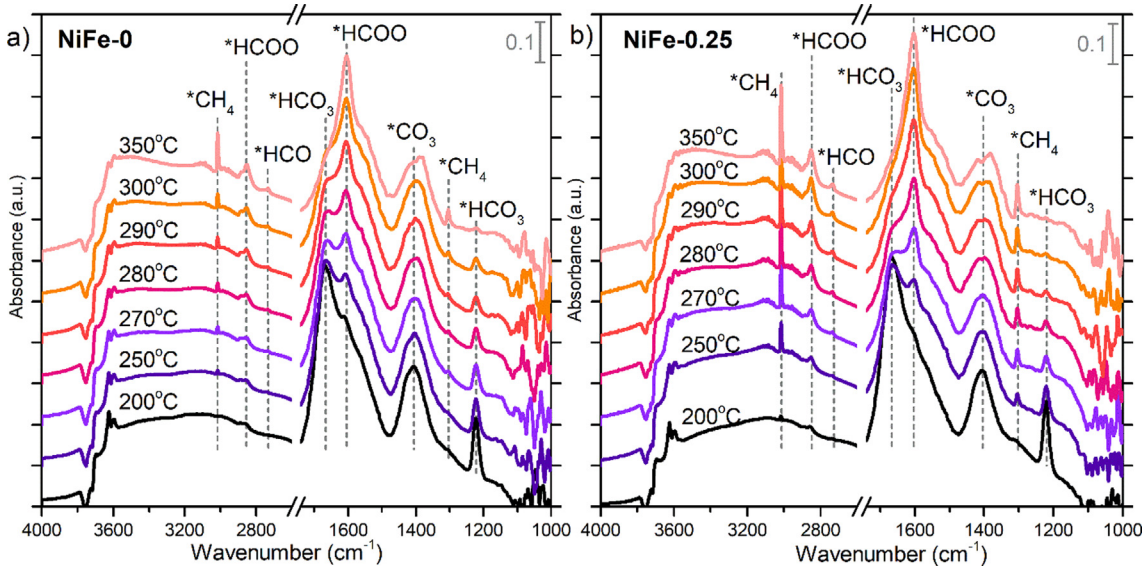

Fig. 8. *In situ* DRIFTS spectra of (a) NiFe-0 and (b) NiFe-0.25 catalysts under CO_2 methanation condition ($CO_2/H_2/N_2$ vol.% = 1/4/5) at increasing temperatures.

assumed to follow the decomposition $*HCO_3 \leftrightarrow *HCOO+*O$. It is also possible that CO_2 was directly hydrogenated $*CO_2+*H \leftrightarrow *HCOO$ at elevated temperature, thus $*HCO_3$ formation was bypassed. *HCOO and *HCO could be the key intermediates in the reaction pathway of CO_2 methanation, while the RWGS could occur via direct CO_2 dissociation since gaseous CO species was found on Fe-rich (NiFe-0.5) catalyst during CO_2 adsorption and methanation (**Figure S8 and S9**). Based on the relative intensity of *in situ* DRIFTS spectra, it further revealed that NiFe alloy could accelerate the formation of *HCOO and *HCO intermediates compared to the monometallic (NiFe-0) catalyst (**Figure S10**). *HCOO formation rate would be promoted by increasing Fe content (NiFe-0.5 > NiFe-0.25 > NiFe-0). However, the production rate of *HCO and CH_4 did not follow this trend (NiFe-0.25 > NiFe-0.5 > NiFe-0). Moreover, because Fe-based catalysts are active for the RWGS reaction [49,50], tuning Fe content is therefore of great importance to achieve the best performance of NiFe alloy catalysts for CO_2 methanation. The transformation of $*HCOO \rightarrow *HCO \rightarrow *CH_4$ could be the key to decipher the promoting effect of Fe in the NiFe alloy catalysts.

3.6. DFT simulations

To further unravel the reaction mechanisms and the higher activity of NiFe alloy compared to monometallic Ni catalysts in CO_2 methanation, DFT calculations were performed on the Ni (111) and Ni4Fe(111) (representing NiFe-0 and NiFe-0.25 catalysts, respectively, as shown in **Figure S11**). Energetics of elementary reactions and the desorption energy of adsorbed species are presented in **Table S3** and **Table S4**, together with the stable geometries of reaction intermediates and its coordinates (**Figure S12 and S13** and **Table S5**).

3.6.1. H_2 dissociation and diffusion

The dissociation of H_2 and diffusion of *H atom on the surface of catalyst directly determine whether the catalyst can provide

enough *H atom for CO_2 methanation. Our calculation shows that the activation energy (E_a) for the dissociation of H_2 on Ni(1 1 1) and Ni4Fe(1 1 1) was estimated to be 1.6, 2.3 (H_2 adsorbed on Fe), and 4.7 (H_2 adsorbed on Ni) kcal mol^{-1}, respectively (Fig. 9.**a**). This implies that H_2 dissociation was facile on these two catalysts. The reaction energy (ΔE) for H_2 dissociation was between −19.2 to −30 kcal mol^{-1}, thus it can be speculated that the formed *H atoms were relatively stable on both catalysts. The diffusion barriers for *H atom on Ni(1 1 1) and Ni4Fe(1 1 1) were estimated to be 12.0 and 16.0 kcal mol^{-1}, respectively (Fig. 9.**b**). This indicates that the diffusion of *H atoms was relatively easy on both catalysts, suggesting the sufficient availability of *H atoms for CO_2 methanation.

3.6.2. CO_2 methanation on Ni and NiFe alloy surface

Based on the *in situ* DRIFTS observation and literature data [51], possible pathways for CO_2 hydrogenation to CH_4 and CO are proposed in Fig. 10. The initial step of CO_2 hydrogenation could occur on either O-terminal to produce *COOH (carboxyl pathway) or C-terminal to produce *HCOO (formate pathway). In the carboxyl pathway, *COOH was dissociated into *CO and *OH, which could be further hydrogenated to produce water or to yield *HCO intermediates. In the formate pathway, *HCOO could directly dissociate to *HCO and *O. The direct dissociation of CO_2 to *CO and *O is also possible. The C-O bond of $*CO_2$ could split to form adsorbed *CO and *O, which underwent hydrogenation to either *HCO+*O following the formate pathway or *CO+*OH following the carboxyl pathway. It is noteworthy that *COH can also be formed from *CO hydrogenation. However, it was not included in our study because *HCO (also written as *CHO) formation was more favorable [52]. It could be assumed that *HCO is the key intermediate in the initial hydrogenation of CO_2, in agreement with literature and the *in situ* DRIFTS study [16,53].

*HCO intermediate can transform to *CHOH, $*H_2CO$, or *CH as intermediates, which could be further hydrogenated to CH_4. It was reported that *HCO dissociation (*HCO↔*CH+*O) was the most favorable pathway amongst others [16,52]. As illustrated in Fig. 10, *CH species underwent sequential hydrogenation reactions to $*CH_2$, $*CH_3$ and eventually $*CH_4$. Likewise, surface *O removal was carried out by two steps of hydrogenation to water. Finally, $*H_2O$ and $*CH_4$ desorbed as gaseous products. Beside CO_2 methanation, the RWGS reaction can occur simultaneously and its mechanism can also be understood by DFT calculations. The side reaction could follow either carboxyl pathway or direct CO_2 dissociation pathway since the dissociated *CO species (cyan route in Fig. 10) could desorb as a gaseous product while surface *O and *OH were removed as water.

The energy diagram of *HCO formation via COOH route with a partial contribution from direct CO_2 dissociation is presented in Fig. 11. On Ni surface, the energy barrier for *COOH formation from $*CO_2$ was calculated to be 12.3 kcal mol^{-1}, while it required 23.9 kcal mol^{-1} for the splitting of *CO and *O. In contrast, *COOH formation had a higher energy barrier (E_a = 20 kcal mol^{-1}) than that of $*CO_2$ direct dissociation on Ni4Fe surface (E_a = 16.3 kcal mo l^{-1}). Therefore, the NiFe alloy surface promoted the dissociation of $*CO_2$, consistent with Kim *et al.* [34] and the *in situ* CO_2 adsorption study.

However, the subsequent hydrogenation of *O at (*CO+*O) state was difficult on both surfaces (E_a of 31.1 and 37.6 kcal mol^{-1} for Ni and Ni4Fe, respectively). Therefore, $*CO_2$→*CO→*HCO transformation can occur easier via the COOH pathway rather than via the direct dissociation. *CO+*H↔*HCO was the rate-determining step (RDS) for the formation of *HCO via COOH route. The activation energy of this reaction was 37.7 kcal mol^{-1} on Ni and 39.5 kcal mol^{-1} on Ni4Fe catalysts. Notably, the hydrogenation of *CO was much less favorable compared to the reverse reaction on both surfaces. The *HCO intermediate was not stable and preferred to decompose back to *CO since the energy barrier of *HCO formation was much higher than its dissociation. It suggests that the RWGS reaction has likely occurred following the COOH pathway. However, the desorption energy of *CO was calculated to be 59.7 kcal mol^{-1} on Ni and 58.1 kcal mol^{-1} on Ni4Fe surface. Hence, CO desorption was very difficult due to the strong binding of *CO to the metallic surfaces. While steadily adsorbed *CO would not contribute to the production of CH_4 via *HCO, it would occupy the active sites, consequently, cause catalytic deactivation during reaction. In our study, *CO was formed and desorbed easier on NiFe alloy compared to the Ni surface in both experimental and theoretical studies. This could explain the more stable performance of NiFe-0.25 compared to NiFe-0 catalyst in the long-term test.

Fig. 12 illustrates the energy diagram of *HCO formation via HCOO route and direct CO_2 dissociation pathway. In the dissociation pathway, the hydrogenation of *CO to *HCO had a very high energy barrier for both Ni (E_a = 38.6 kcal mol^{-1}) and Ni4Fe catalysts (E_a = 39.3 kcal mol^{-1}). Indeed, *CO hydrogenation was rather difficult via either COOH or direct dissociation pathway with E_a of roughly 38–40 kcal mol^{-1}. It is also noticeable that the reaction was not facilitated on Ni4Fe alloy surface. In contrast, $*CO_2$ was more likely to be hydrogenated to *HCOO with a moderate E_a of 15.2–16.0 kcal mol^{-1} on both surfaces. For the C-O bond cleavage of *HCOO to *HCO, an energy barrier of 32.3 kcal mol^{-1} was needed to overcome for monometallic Ni, but it required only 8.5 kcal mol^{-1} for Ni4Fe alloy. Therefore, the transformation of $*CO_2$→*HCOO→

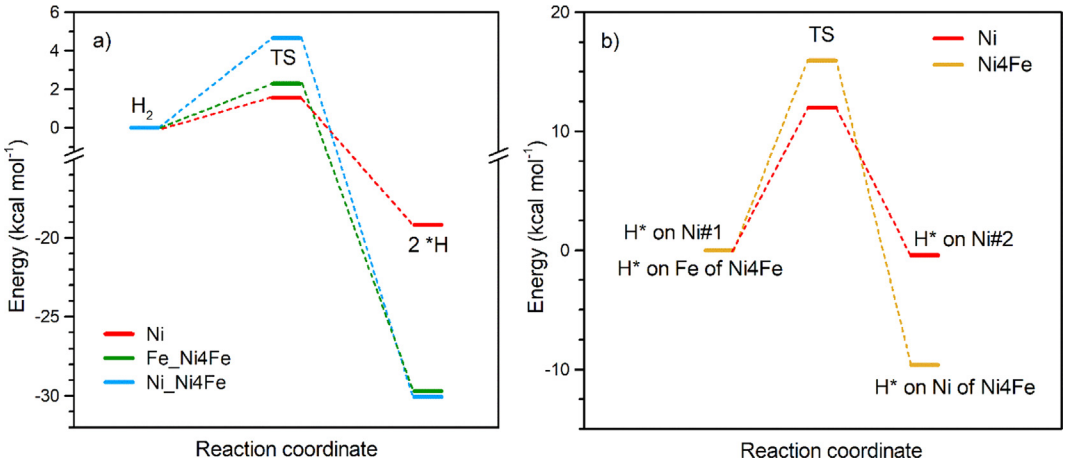

Fig. 9. (a) H_2 dissociation pathway and (b) *H diffusion pathway on Ni and Ni4Fe surface.

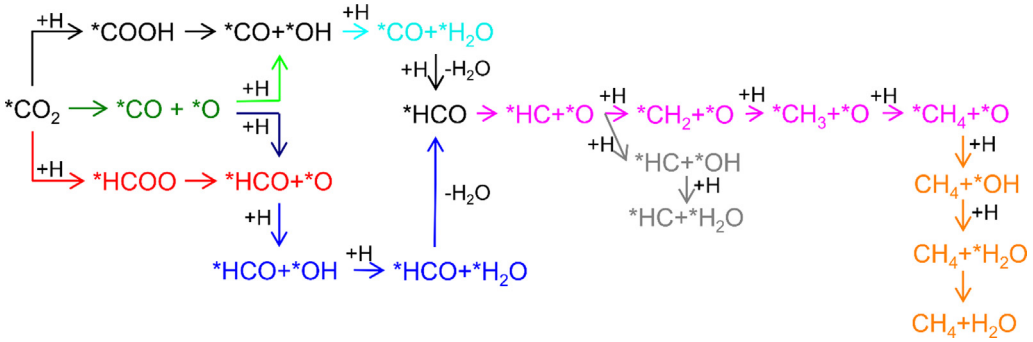

Fig. 10. Plausible reaction schemes of CO_2 methanation.

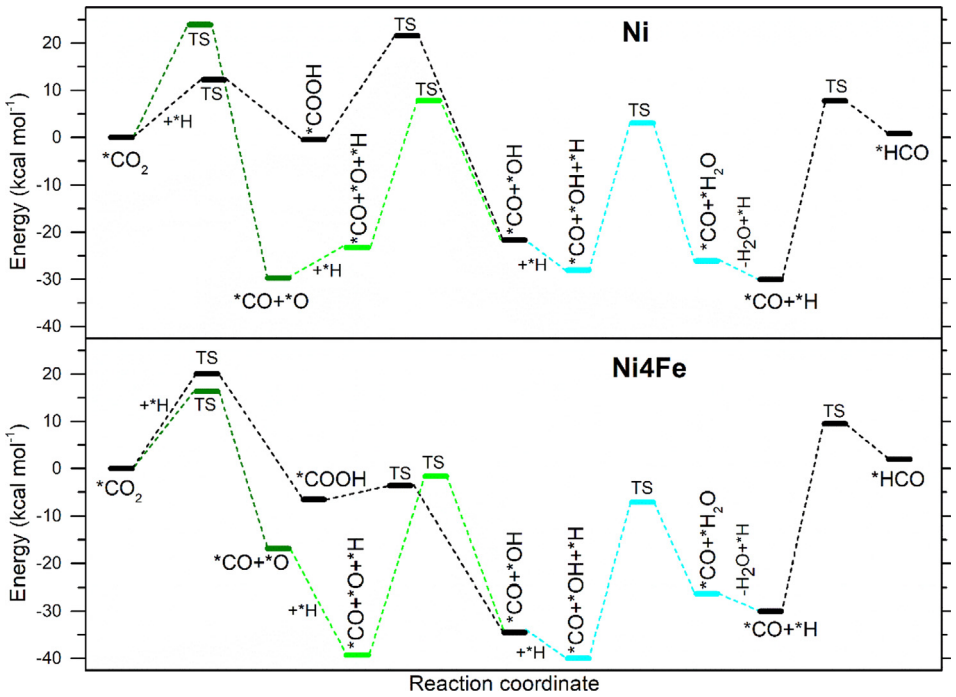

Fig. 11. Energy diagram for the formation of *HCO via COOH pathway and CO_2 direct dissociation pathway on Ni(1 1 1) and Ni4Fe(1 1 1).

*HCO was more facile than that of $*CO_2 \rightarrow *CO \rightarrow *HCO$ regardless of the catalytic systems, and *HCO was formed much easier on Ni4Fe alloy surface than on Ni surface. *HCOO appeared to be more stable on Ni surface and could be detected experimentally [6], while Ni4Fe alloy was more active to produce *HCO. This could explain the higher formation rate of *HCOO and *HCO observed in the *in situ* DRIFTS study.

Fig. 13 illustrates the energy diagram of $*HCO \rightarrow *CH_4$ transformation for both catalyst surfaces. It shows that the decomposition of *HCO occurred with a moderate E_a of 23.5 kcal mol^{-1} on Ni surface and 22.6 kcal mol^{-1} on Ni4Fe surface. Alloy surface promoted the formation of *CH and *O better than Ni surface. When (*CH+*O) reacted with *H, either $*CH_2$ or *OH could be formed. While *CH further yielded $*CH_4$ (Fig. 13), water could also be produced (**Figure S14**, gray pathway). *CH and $*CH_3$ were other stable adsorbed species on the metal surfaces. *CH could easily overcome small barriers of approximately 15 kcal mol^{-1} to form $*CH_2$ and $*CH_3$, while the formation of $*CH_4$ from $*CH_3$ required very high activation energy of 26.2–26.9 kcal mol^{-1} on both surfaces, which could be assumed to be the RDS of $*HCO \rightarrow *CH_4$ transformation.

Finally, $*CH_4$ was desorbed to gaseous CH_4 as product with a desorption energy of 8.27 and 19.14 kcal mol^{-1} from Ni and Ni4Fe surface, respectively. Indeed, $*CH_4$ was more strongly bound on Ni4Fe alloy surface than on Ni surface. According to Young, reactions with a barrier of 21 kcal mol^{-1} or less can readily occur at room temperature [54]. Accordingly, CH_4 could easily desorb from both catalytic surfaces. The energy diagram for water produced from *O at ($*CH_4$+*O) state is also presented in **Figure S14** (orange pathway). The removal of *O by two steps hydrogenation is crucial because not only the active sites would be free from occupied *O, but $*H_2O$ would also be produced as a product from both RWGS and CO_2 methanation. The formation of $*H_2O$ via $*OH+*H \leftrightarrow *H_2O$ required significantly high activation energy compared to the formation of $*CH_4$, which agreed with Zhang *et al.* [55]. However, $*H_2O$ could also be formed via $*OH+*OH \leftrightarrow *H_2O+*O$ at very low activation energy of 3.4 kcal mol^{-1} and 1.2 kcal mol^{-1} on Ni and Ni4Fe surface, respectively.

Microkinetic modeling on Ni(1 1 1) surface reported that $HCO^* \leftrightarrow CH^*+O^*$ was the main RDS for CO_2 methanation [56]. As mentioned above, the decomposition of *HCO was better facilitated on Ni4Fe than on Ni surface due to a lower energy barrier. Accord-

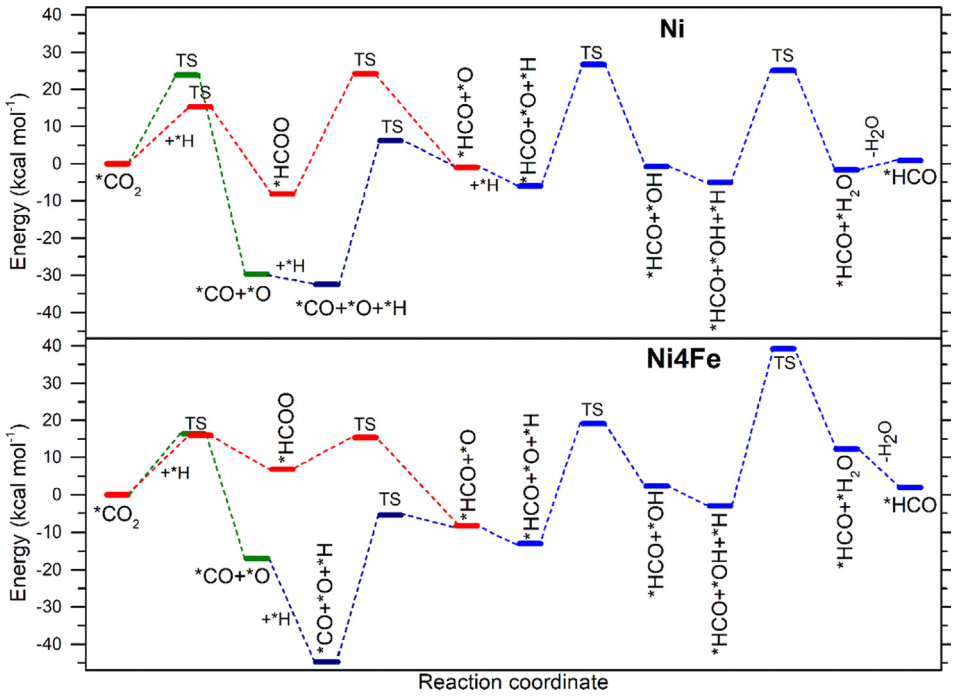

Fig. 12. Energy diagram for the formation of *HCO via HCOO pathway and CO_2 direct dissociation pathway on Ni(1 1 1) and Ni4Fe(1 1 1).

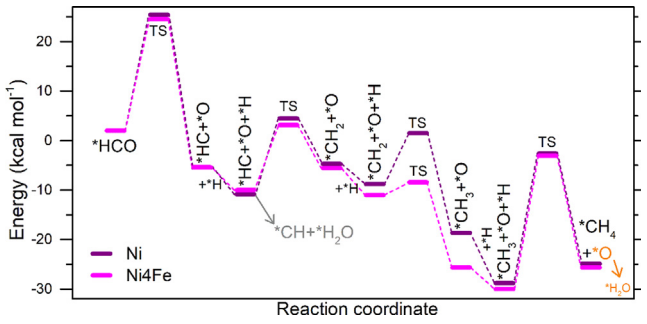

Fig. 13. Energy diagram for the formation of *CH_4 from *HCO on Ni(1 1 1) and Ni4Fe (1 1 1).

ing to our DFT calculations, *HCO formation via *HCOO was the most energetically favorable pathway, especially on Ni4Fe alloy surface. Fe alloying with Ni at a certain molar ratio could result in an effective catalytic system that reduced the energy barrier for *CO_2 hydrogenation. The alloy surface further facilitated the dissociation of *HCO to *CH, thus accelerated the *CH_4 formation.

On the other hand, the desorption of *CO was easier on Ni4Fe than on Ni surface. While stably adsorbed *CO could block available sites on the surface, *O and *H_2O were also possible to occupy the Ni and NiFe active sites. The removal of *O via two-step hydrogenation to water is important. It was recently proposed that Fe could hinder Ni hydroxylation thus catalyst deactivation since it could be the preferential site for water production [57,58]. However, our DFT results showed similar energy is required for·H_2O formation and desorption on both Ni and alloy surfaces. Further studies on the deactivation mechanism of Ni and NiFe alloy are highly recommended.

4. Conclusions

Bimetallic NiFe on $(Mg,Al)O_x$ support catalysts were derived from HT precursors prepared by rapid coprecipitation method. Extensive characterizations verified that small NiFe alloy particles (6–7 nm) were formed upon reduction at 600 °C. The NiFe alloy catalysts could enhance the activity, selectivity towards CH_4, and stability in CO_2 methanation, particularly at low temperatures of 250–350 °C compared to monometallic Ni catalysts. However, the amount of Fe addition significantly influenced the catalytic behavior in which an optimal Fe/Ni molar ratio of 0.25 would obtain the highest CH_4 yield. Both *in situ* DRIFTS observation and DFT calculations showed that CO_2 activation via hydrogenation to *HCOO was more preferred than its direct dissociation on both Ni and NiFe alloy surfaces. *CO_2→*HCOO→*HCO→*CH→*CH_4 transformation was considered as the most energetically favorable pathway for CO_2 methanation. The superior catalytic performance of NiFe-0.25 alloy catalysts could be explained by the lower energy barrier for CH_4 formation. At the same time, weak interaction with adsorbed *CO species maintained the free active sites and prolonged the catalytic stability. Our study has provided additional insights into the formate pathway and the promoting effect of Fe for Ni-based catalysts in CO_2 methanation. The NiFe alloy catalyst is a plausible industrial catalyst because it improved the efficiency and lowered the cost of traditional Ni-based catalysts, which are important factors for the development of the PtG process.

Declaration of Competing Interest

The authors declared that there is no conflict of interest.

Acknowledgments

This research has received funding from the Norwegian Ministry of Education and Research and the Plogen program from Valide AS (Norway). JZ and GZ would like to acknowledge the National Natural Science Foundation of China (21902019) and the Fundamental Research Funds for Central Universities (DUT20RC(5)002).

Appendix A. Supplementary data

Supplementary data to this article can be found online at https://doi.org/10.1016/j.jcat.2020.10.018.

References

[1] J. Artz, T.E. Müller, K. Thenert, J. Kleinekorte, R. Meys, A. Sternberg, A. Bardow, W. Leitner, Sustainable Conversion of Carbon Dioxide: An Integrated Review of Catalysis and Life Cycle Assessment, Chem. Rev. 118 (2018) 434–504.

[2] P. Sabatier, J.-B. Senderens, Nouvelles syntheses du methane, Comptes Rendus Des Séances De L'Académie Des Sciences, Section VI –, Chimie 134 (1902) 514–516.

[3] C. Vogt, M. Monai, G.J. Kramer, B.M. Weckhuysen, The renaissance of the Sabatier reaction and its applications on Earth and in space, Nat. Catal. 2 (2019) 188–197.

[4] M. Bailera, P. Lisbona, L.M. Romeo, S. Espatolero, Power to Gas projects review: Lab, pilot and demo plants for storing renewable energy and CO2, Renew. Sustain. Energy Rev. 69 (2017) 292–312.

[5] S. Rönsch, J. Schneider, S. Matthischke, M. Schlüter, M. Götz, J. Lefebvre, P. Prabhakaran, S. Bajohr, Review on methanation – From fundamentals to current projects, Fuel 166 (2016) 276–296.

[6] E. Vesselli, M. Rizzi, L. De Rogatis, X. Ding, A. Baraldi, G. Comelli, L. Savio, L. Vattuone, M. Rocca, P. Fornasiero, A. Baldereschi, M. Peressi, Hydrogen-Assisted Transformation of CO2 on Nickel: The Role of Formate and Carbon Monoxide, The Journal of Physical Chemistry Letters 1 (2010) 402–406.

[7] M.A.A. Aziz, A.A. Jalil, S. Triwahyono, A. Ahmad, CO2 methanation over heterogeneous catalysts: recent progress and future prospects, Green Chem. 17 (2015) 2647–2663.

[8] M. Younas, L. Loong Kong, M.J.K. Bashir, H. Nadeem, A. Shehzad, S. Sethupathi, Recent Advancements, Fundamental Challenges, and Opportunities in Catalytic Methanation of CO2, Energy Fuels 30 (2016) 8815–8831.

[9] M.P. Andersson, T. Bligaard, A. Kustov, K.E. Larsen, J. Greeley, T. Johannessen, C. H. Christensen, J.K. Nørskov, Toward computational screening in heterogeneous catalysis: Pareto-optimal methanation catalysts, J. Catal. 239 (2006) 501–506.

[10] A.L. Kustov, A.M. Frey, K.E. Larsen, T. Johannessen, J.K. Nørskov, C.H. Christensen, CO methanation over supported bimetallic Ni–Fe catalysts: From computational studies towards catalyst optimization, Appl. Catal. A 320 (2007) 98–104.

[11] J. Sehested, K.E. Larsen, A.L. Kustov, A.M. Frey, T. Johannessen, T. Bligaard, M.P. Andersson, J.K. Nørskov, C.H. Christensen, Discovery of technical methanation catalysts based on computational screening, Top. Catal. 45 (2007) 9–13.

[12] S. Hwang, U.G. Hong, J. Lee, J.H. Baik, D.J. Koh, H. Lim, I.K. Song, Methanation of Carbon Dioxide Over Mesoporous Nickel–M–Alumina (M = Fe, Zr, Ni, Y, and Mg) Xerogel Catalysts: Effect of Second Metal, Catal. Lett. 142 (2012) 860–868.

[13] D. Pandey, G. Deo, Effect of support on the catalytic activity of supported Ni–Fe catalysts for the CO2 methanation reaction, J. Ind. Eng. Chem. 33 (2016) 99–107.

[14] J. Ren, X. Qin, J.-Z. Yang, Z.-F. Qin, H.-L. Guo, J.-Y. Lin, Z. Li, Methanation of carbon dioxide over Ni–M/ZrO2 (M=Fe Co, Cu) catalysts: Effect of addition of a second metal, Fuel Process. Technol. 137 (2015) 204–211.

[15] D. Pandey, K. Ray, R. Bhardwaj, S. Bojja, K.V.R. Chary, G. Deo, Promotion of unsupported nickel catalyst using iron for CO2 methanation, Int. J. Hydrogen Energy 43 (2018) 4987–5000.

[16] B. Yan, B. Zhao, S. Kattel, Q. Wu, S. Yao, D. Su, J.G. Chen, Tuning CO2 hydrogenation selectivity via metal-oxide interfacial sites, J. Catal. 374 (2019) 60–71.

[17] C. Mebrahtu, F. Krebs, S. Perathoner, S. Abate, G. Centi, R. Palkovits, Hydrotalcite based Ni–Fe/(Mg, Al)Ox catalysts for CO2 methanation – tailoring Fe content for improved CO dissociation, basicity, and particle size, Catal. Sci. Technol. 8 (2018) 1016–1027.

[18] T. Burger, F. Koschany, A. Wenng, O. Thomys, K. Köhler, O. Hinrichsen, Simultaneous activity and stability increase of co-precipitated Ni–Al CO2 methanation catalysts by synergistic effects of Fe and Mn promoters, Catal. Sci. Technol. 8 (2018) 5920–5932.

[19] B. Mutz, M. Belimov, W. Wang, P. Sprenger, M.-A. Serrer, D. Wang, P. Pfeifer, W. Kleist, J.-D. Grunwaldt, Potential of an Alumina-Supported Ni3Fe Catalyst in the Methanation of CO2: Impact of Alloy Formation on Activity and Stability, ACS Catal. 7 (2017) 6802–6814.

[20] T. Burger, F. Koschany, O. Thomys, K. Köhler, O. Hinrichsen, CO2 methanation over Fe- and Mn-promoted co-precipitated Ni-Al catalysts: Synthesis, characterization and catalysis study, Appl. Catal. A 558 (2018) 44–54.

[21] H.L. Huynh, W.M. Tucho, X. Yu, Z. Yu, Synthetic natural gas production from CO2 and renewable H2: Towards large-scale production of Ni–Fe alloy catalysts for commercialization, J. Cleaner Prod. 121720 (2020).

[22] D.A.M. Monti, A. Baiker, Temperature-programmed reduction. Parametric sensitivity and estimation of kinetic parameters, J. Catal. 83 (1983) 323–335.

[23] B. Delley, An all-electron numerical method for solving the local density functional for polyatomic molecules, J. Chem. Phys. 92 (1990) 508–517.

[24] B. Delley, From molecules to solids with the DMol3 approach, J. Chem. Phys. 113 (2000) 7756–7764.

[25] J.P. Perdew, K. Burke, M. Ernzerhof, Generalized Gradient Approximation Made Simple, Phys. Rev. Lett. 77 (1996) 3865–3868.

[26] M.V. Frash, V.B. Kazansky, A.M. Rigby, R.A. van Santen, Cracking of Hydrocarbons on Zeolite Catalysts: Density Functional and Hartree−Fock Calculations on the Mechanism of the β-Scission Reaction, J. Phys. Chem. B 102 (1998) 2232–2238.

[27] K. Mette, S. Kühl, H. Düdder, K. Kähler, A. Tarasov, M. Muhler, M. Behrens, Stable Performance of Ni Catalysts in the Dry Reforming of Methane at High Temperatures for the Efficient Conversion of CO2 into Syngas, ChemCatChem 6 (2014) 100–104.

[28] K.S. Sing, D.H. Everett, R.A. Haul, L. Moscou, R.A. Pierotti, R. J., T. Siemieniewska, Reporting Physisorption Data for Gas/Solid Systems, in: Handbook of Heterogeneous Catalysis, 2008.

[29] D. Beierlein, D. Häussermann, M. Pfeifer, T. Schwarz, K. Stöwe, Y. Traa, E. Klemm, Is the CO2 methanation on highly loaded Ni-Al2O3 catalysts really structure-sensitive?, Appl. Catal. B 247 (2019) 200–219.

[30] M.-M. Millet, A.V. Tarasov, F. Girgsdies, G. Algara-Siller, R. Schlögl, E. Frei, Highly Dispersed Ni0/NixMg1−xO Catalysts Derived from Solid Solutions: How Metal and Support Control the CO2 Hydrogenation, ACS Catal. 9 (2019) 8534–8546.

[31] S.-H. Kang, J.-H. Ryu, J.-H. Kim, S.-J. Seo, Y.-D. Yoo, P.S. Sai Prasad, H.-J. Lim, C.-D. Byun, Co-methanation of CO and CO2 on the NiX-Fe1−X/Al2O3 catalysts; effect of Fe contents, Korean J. Chem. Eng. 28 (2011) 2282–2286.

[32] R. Brown, M.E. Cooper, D.A. Whan, Temperature programmed reduction of alumina-supported iron, cobalt and nickel bimetallic catalysts, Applied Catalysis 3 (1982) 177–186.

[33] X. Ge, M. Li, J. Shen, The Reduction of Mg–Fe–O and Mg–Fe–Al–O Complex Oxides Studied by Temperature-Programmed Reduction Combined with in Situ Mössbauer Spectroscopy, J. Solid State Chem. 161 (2001) 38–44.

[34] S.M. Kim, P.M. Abdala, T. Margossian, D. Hosseini, L. Foppa, A. Armutlulu, W. van Beek, A. Comas-Vives, C. Copéret, C. Müller, Cooperativity and Dynamics Increase the Performance of NiFe Dry Reforming Catalysts, J. Am. Chem. Soc. 139 (2017) 1937–1949.

[35] D. Pandey, G. Deo, Promotional effects in alumina and silica supported bimetallic Ni–Fe catalysts during CO2 hydrogenation, J. Mol. Catal. A: Chem. 382 (2014) 23–30.

[36] S.A. Theofanidis, V.V. Galvita, H. Poelman, G.B. Marin, Enhanced Carbon-Resistant Dry Reforming Fe-Ni Catalyst: Role of Fe, ACS Catal. 5 (2015) 3028–3039.

[37] L. He, Q. Lin, Y. Liu, Y. Huang, Unique catalysis of Ni-Al hydrotalcite derived catalyst in CO2 methanation: cooperative effect between Ni nanoparticles and a basic support, Journal of Energy Chemistry 23 (2014) 587–592.

[38] P.A.U. Aldana, F. Ocampo, K. Kobl, B. Louis, F. Thibault-Starzyk, M. Daturi, P. Bazin, S. Thomas, A.C. Roger, Catalytic CO2 valorization into CH4 on Ni-based ceria-zirconia, Reaction mechanism by operando IR spectroscopy, Catalysis Today 215 (2013) 201–207.

[39] M.B. Jensen, S. Morandi, F. Prinetto, A.O. Sjåstad, U. Olsbye, G. Ghiotti, FT-IR characterization of supported Ni-catalysts: Influence of different supports on the metal phase properties, Catal. Today 197 (2012) 38–49.

[40] K. Hadjiivanov, Chapter Two - Identification and Characterization of Surface Hydroxyl Groups by Infrared Spectroscopy, in: F.C. Jentoft (Ed.), Advances in Catalysis, Academic Press, 2014, pp. 99–318.

[41] J.I. Di Cosimo, V.K. Díez, M. Xu, E. Iglesia, C.R. Apesteguía, Structure and Surface and Catalytic Properties of Mg-Al Basic Oxides, J. Catal. 178 (1998) 499–510.

[42] F. Solymosi, A. Erdöhelyi, T. Bánsági, Infrared study of the surface interaction between H2 and CO2 over rhodium on various supports, J. Chem. Soc., Faraday Trans. 1 F 77 (1981) 2645–2657.

[43] G. Busca, V. Lorenzelli, Infrared spectroscopic identification of species arising from reactive adsorption of carbon oxides on metal oxide surfaces, Materials Chemistry 7 (1982) 89–126.

[44] S.R. Tong, L.Y. Wu, M.F. Ge, W.G. Wang, Z.F. Pu, Heterogeneous chemistry of monocarboxylic acids on alpha-Al2O3 at different relative humidities, Atmos. Chem. Phys. 10 (2010) 7561–7574.

[45] Y. Wang, Y. Su, M. Zhu, L. Kang, Mechanism of CO methanation on the Ni4/γ-Al2O3 and Ni3Fe/γ-Al2O3 catalysts: A density functional theory study, Int. J. Hydrogen Energy 40 (2015) 8864–8876.

[46] K. Ito, H.J. Bernstein, The Vibrational Spectra Of The Formate, Acetate, And Oxalate Ions, Can. J. Chem. 34 (1956) 170–178.

[47] J. Raskó, J. Kiss, Adsorption and surface reactions of acetaldehyde on alumina-supported noble metal catalysts, Catal. Lett. 101 (2005) 71–77.

[48] J. Coates, Interpretation of Infrared Spectra, A Practical Approach, in: Encyclopedia of Analytical Chemistry, Wiley, 2006.

[49] D.H. Kim, S.W. Han, H.S. Yoon, Y.D. Kim, Reverse water gas shift reaction catalyzed by Fe nanoparticles with high catalytic activity and stability, J. Ind. Eng. Chem. 23 (2015) 67–71.

[50] C.-S. Chen, W.-H. Cheng, S.-S. Lin, Study of iron-promoted Cu/SiO2 catalyst on high temperature reverse water gas shift reaction, Appl. Catal. A 257 (2004) 97–106.

[51] S. Kattel, P. Liu, J.G. Chen, Tuning Selectivity of CO2 Hydrogenation Reactions at the Metal/Oxide Interface, J. Am. Chem. Soc. 139 (2017) 9739–9754.

[52] E.B. Sterk, CO2 methanation over Ni and its structure sensitivity. A computational study, Inorganic Chemistry and Catalysis, Utrecht University, 2018.

[53] W. Zhen, F. Gao, B. Tian, P. Ding, Y. Deng, Z. Li, H. Gao, G. Lu, Enhancing activity for carbon dioxide methanation by encapsulating (111) facet Ni particle in metal–organic frameworks at low temperature, J. Catal. 348 (2017) 200–211.

[54] D. Young, Finding Transition Structures, in: Computational Chemistry: A Practical Guide for Applying Techniques to Real World Problems, John Wiley & Sons, Inc., 2002, pp. 145-158.
[55] M. Zhang, B. Zijlstra, I.A.W. Filot, F. Li, H. Wang, J. Li, E.J.M. Hensen, A theoretical study of the reverse water-gas shift reaction on Ni(111) and Ni (311) surfaces, The Canadian Journal of Chemical Engineering 98 (2020) 740–748.
[56] C. Vogt, M. Monai, E.B. Sterk, J. Palle, A.E.M. Melcherts, B. Zijlstra, E. Groeneveld, P.H. Berben, J.M. Boereboom, E.J.M. Hensen, F. Meirer, I.A.W. Filot, B.M. Weckhuysen, Understanding carbon dioxide activation and carbon–carbon coupling over nickel, Nat. Commun. 10 (2019) 5330.
[57] C. Mebrahtu, S. Perathoner, G. Giorgianni, S. Chen, G. Centi, F. Krebs, R. Palkovits, S. Abate, Deactivation mechanism of hydrotalcite-derived Ni–AlOx catalysts during low-temperature CO2 methanation via Ni-hydroxide formation and the role of Fe in limiting this effect, Catal. Sci. Technol. 9 (2019) 4023–4035.
[58] G. Giorgianni, C. Mebrahtu, M.E. Schuster, A.I. Large, G. Held, P. Ferrer, F. Venturini, D. Grinter, R. Palkovits, S. Perathoner, G. Centi, S. Abate, R. Arrigo, Elucidating the mechanism of the CO2 methanation reaction over Ni–Fe hydrotalcite-derived catalysts via surface-sensitive in situ XPS and NEXAFS, PCCP (2020).